Available online at www.sciencedirect.com
SCIENCE DIRECT®
Journal of Computational Physics 212 (2006) 124–149
JOURNAL OF COMPUTATIONAL PHYSICS
www.elsevier.com/locate/jcp

A shock-capturing SPH scheme based on adaptive kernel estimation

Leonardo Di G. Sigalotti [a,*], Hender López [a], Arnaldo Donoso [a], Eloy Sira [a], Jaime Klapp [b]

[a] *Centro de Física, Instituto Venezolano de Investigaciones Científicas, IVIC, Apartado 21827, Caracas 1020A, Venezuela*
[b] *Instituto Nacional de Investigaciones Nucleares, ININ, Km. 36.5, Carretera México-Toluca, Ocoyoacac 52045, Estado de México, México*

Received 21 February 2005; received in revised form 25 May 2005; accepted 29 June 2005
Available online 10 August 2005

Abstract

Here we report a method that converts standard smoothed particle hydrodynamics (SPH) into a working shock-capturing scheme without relying on solutions to the Riemann problem. Unlike existing adaptive SPH simulations, the present scheme is based on an *adaptive kernel estimation* of the density, which combines intrinsic features of both the kernel and nearest neighbor approaches in a way that the amount of smoothing required in low-density regions is effectively controlled. Symmetrized SPH representations of the gas dynamic equations along with the usual kernel summation for the density are used to guarantee variational consistency. Implementation of the adaptive kernel estimation involves a very simple procedure and allows for a unique scheme that handles strong shocks and rarefactions the same way. Since it represents a general improvement of the integral interpolation on scattered data, it is also applicable to other fluid-dynamic models. When the method is applied to supersonic compressible flows with sharp discontinuities, as in the classical one-dimensional shock-tube problem and its variants, the accuracy of the results is comparable, and in most cases superior, to that obtained from high quality Godunov-type methods and SPH formulations based on Riemann solutions. The extension of the method to two- and three-space dimensions is straightforward. In particular, for the two-dimensional cylindrical Noh's shock implosion and Sedov point explosion problems the present scheme produces much better results than those obtained with conventional SPH codes.

Keywords: SPH: Godunov's method; Lagrangian: Particle method, numerical methods, conservation laws, ideal compressible flows

* Corresponding author. Tel.: +58 212 504 1369; fax: +58 212 504 1148.
E-mail addresses: lsigalot@ivic.ve (L. Di G. Sigalotti), hlopez@ivic.ve (H. López), arnaldo@ivic.ve (A. Donoso), easira@ivic.ve (E. Sira), klapp@nuclear.inin.mx (J. Klapp).

0021-9991/$ - see front matter
doi:10.1016/j.jcp.2005.06.016

1. Introduction

The method of smoothed particle hydrodynamics (SPH) was originally devised to simulate a wide variety of problems in astrophysics involving the three-dimensional motion of compressible fluid masses at different spatial scales [1,2]. In general, SPH is a particle method that relies on a Lagrangian description of the fluid, and unlike ordinary finite-difference (FD) methods, it is gridless and easy to handle under complicated physics and arbitrary geometries. For details on the general aspects of SPH and its applications to astrophysical and cosmological flows, see the review by Monaghan [3] and references therein. Because of its simplicity and robustness, it has rapidly become a useful tool for applications in numerous other areas, including fluid dynamics [4–9], magnetohydrodynamics [10–12], free surface and interfacial flows [13–16], multi-phase flows [17], and computational mechanics, where it has primarily been employed to study the response of elastic bodies to induced large deformations [18–20], high-velocity impacts, penetration, and shock damage in solids [21–28], and explosion phenomena [29,30].

Since its invention, SPH has been the subject of extensive research to address major technical difficulties associated with it. As a result, a large amount of proposed formulations exists in the literature that improve the accuracy of the approximation at boundaries [31–33] and near sharp fluid discontinuities [34–37], address the tensile instability [20,32,38], and solve for inconsistency and momentum preservation problems [39,40]. In particular, when conventional SPH is applied to model supersonic flows of an ideal gas over a step, the resulting shock fronts are not as sharp as those obtained with high quality Godunov-type schemes based on solutions to the Riemann problem. In general, SPH gives shock profiles that appear blurred by viscosity and significantly much broader than those for exact, or well approximated, Riemann solutions.

Attempts to improve the performance of SPH on unsteady compressible flows with strong shocks were first reported by Monaghan [34], and more recently, by Inutsuka [35] and Cha and Whitworth [36]. The former author found that working with the specific total energy equation rather than the specific internal energy equation and relating the dissipative terms in the SPH equations with those appearing in Riemann formulations, may significantly improve the accuracy of SPH in reproducing the analytical solutions of the one-dimensional (1D) classical Sod's [41] shock tube, blast wave [42], and wall shock problems. The method was also seen to perform well for test problems where many shock-capturing FD schemes could fail, as is the case for a slowly moving shock wave [43] or for the Sjögreen test [44] in which two strong rarefaction waves move apart leaving behind a region of very low density. In addition to working with an equation for the total energy, the other fundamental change operated by Monaghan [34], with respect to conventional SPH schemes, lies on the form used for the artificial viscosity terms. In particular, any pair of interacting particles is treated as the left and right states of the Riemann problem, with the changes between the two particles being taken along the line joining them. In this way, a signal velocity can be constructed in analogy to the form of the eigenvalues of the 1D Euler equations. The artificial viscous acceleration term is then defined as the product of the signal velocity and the velocity difference between the two particles; the latter quantity serving to approximate the jump in the velocity across characteristics. Similarly, the artificial viscous heating is obtained by multiplying the signal velocity with the corresponding jump in the total energy.

In spite of the high accuracy achieved for the shock-tube problem, a drawback of Monaghan's [34] formulation is that it is not variationally consistent because symmetrized SPH expressions for the pressure forces in the momentum equation and the $\nabla \cdot (pv)$ term in the total energy equation are used in conjunction with a time-integrated solution to the continuity equation rather than with the usual kernel smoothing for the density. According to the analysis of Bonet and Lok [39], an SPH scheme based on symmetrized representations of the equations of motion and energy would be variationally consistent only if the density is calculated using the kernel summation. In addition, Monaghan's [34] scheme is not able to handle strong shocks and rarefactions the same way. This is the case of the continuity equation which was employed in all

Riemann shock simulations with the exception of the Sjögreen test, which demanded the use of the kernel summation for the density to yield accurate results. A further consideration regards the numerically calculated density profiles in the blast wave and wall shock problems, where the postshock value was always in excess of about 10% over the analytical solution.

More involved reformulations of SPH for handling strong shock phenomena were reported independently by Inutsuka [35] and Cha and Whitworth [36]. While both formulations are based on similar SPH representations, in the one proposed by Inutsuka [35], the evolution equations for the particles are obtained in strict conservation form by direct convolution of the exact equations with the kernel function. Evaluation of the spatial integrals is performed by interpolating the square of the specific volume around each pair of particles. In contrast to Monaghan's [34] formulation, the force acting on each particle is determined by solving the Riemann problem in the vicinity of the midpoint between each pair of interacting particles. This procedure is the analogous of that used in Godunov-type schemes where the Riemann problem is solved at each cell interface for calculation of the numerical fluxes. While this SPH formulation effectively relies on solution to the Riemann problem, the results are sensitive to the accuracy of the interpolation used in the numerical convolution. In particular, when a linear interpolation is employed, the pressure profile is affected by the presence of unphysical wiggling at the contact discontinuity in both the shock tube and blast wave problems. The amplitude of the pressure wiggling is only slightly reduced when a cubic spline interpolation is used, implying that a much higher-order approximation would be necessary for evaluating the spatial integrals.

The motivation of this paper is to present a shock-capturing SPH formulation, which is variationally consistent and works equally well for strong and weak shocks as well as for rarefaction waves. The scheme is based on a variant of the adaptive kernel estimation procedure described by Silverman [45]. This class of kernel estimates has the advantage of combining features of both the kernel and nearest neighbor approaches. The basic idea is to construct an estimate consisting of kernels placed at the observed data points in such a way as to allow the window width of the kernels to vary from one point to another. In this procedure, a pilot estimate of the density is first calculated from the usual kernel summation. This yields a pattern of bandwidths, λ_i, corresponding to the various observation points (or particles). The heart of the method consists of defining the λ_i's as some power of the ratio of the pilot estimates of the density over their corresponding geometrical means. In this way, the width of the kernels (or local smoothing length) placed at the observation points is simply $\lambda_i h$. As a final step, the adaptive kernel estimator of the density is evaluated using the $\lambda_i h$'s with the same smoothing kernel summation employed for the pilot estimate. While this procedure has the disadvantage of requiring a recalculation of the pilot estimate for each new value of the smoothing length, the accuracy of the SPH calculation will strongly benefit of the fact that the values of λ_i constructed this way effectively control the amount of smoothing applied to the data, thus allowing the adaptive kernel estimate to behave as a *bona fide* probability density. This is particularly important for density distributions with long tails, where the density is low, and therefore a much broader kernel would be required in the way that the nearest neighbor method does. Note that the above procedure differs from that commonly used in other adaptive SPH calculations [46,47], where a variable smoothing length is enforced by relating the time rate of change of h to that of the density at each observation point via a differential equation.

In contrast to Monaghan's [34] and Inutsuka's [35] formulations, the shock-capturing scheme proposed here does not rely on the Riemann problem as a guide to improve SPH. In fact, it is based on standard symmetrized representations of the SPH equations along with the usual kernel smoothing for the density so that variational consistency of the scheme is guaranteed [39]. As a further remark, there is no need to replace the specific internal energy equation with one for the total energy, and what seems to be more important, the implementation of the adaptive kernel estimation of the density allows for a unique scheme that works equally well for strong shocks and rarefactions. In order to validate the accuracy of the method on unsteady compressible flows, we restrict ourselves to the standard analytic test bed of 1D shock

problems for which the initial hydrodynamical states may be either uniform, as in the usual Riemann shock-tube and its variants, or spatially varying, as in the impulsive shock problem of Zel'dovich and Raizer [48]. The extension of the method to two-dimensions (2D) is also tested for the cylindrical Noh's [49] shock implosion and Sedov [50] point explosion problems.

2. The SPH method

2.1. Fundamental aspects

In SPH, the continuum fluid is represented by a finite set of observation points, or particles, through the use of a smoothing procedure in which the value $\hat{f}(\mathbf{x})$ of a function $f(\mathbf{x})$ at a point $\mathbf{x}$, in the domain Ω, is approximated by the integral interpolant:

$$\hat{f}(\mathbf{x}) = \int_{\Omega} f(\mathbf{x}')W(\mathbf{x}-\mathbf{x}', h)\,\mathrm{d}\mathbf{x}', \tag{1}$$

where $W(\mathbf{x}-\mathbf{x}', h)$ is a smooth (differentiable) function, commonly referred to as the interpolating kernel, and h is the bandwidth of the kernel, or smoothing length, which determines its support. The kernel function is defined such that (i) it mimics the Dirac δ-function in the limit $h \to 0$, (ii) its integral over the domain Ω is exactly unity, and (iii) $W(\mathbf{x}-\mathbf{x}', h) = W(\mathbf{x}'-\mathbf{x}, h)$.

The SPH estimate of the gradient of $f(\mathbf{x})$ at a point $\mathbf{x}$, say $\nabla\hat{f}(\mathbf{x})$, is obtained by using the integral interpolant (1) on $\nabla f(\mathbf{x})$ to yield

$$\nabla\hat{f}(\mathbf{x}) = \int_{\Omega} f(\mathbf{x}')\nabla W(\mathbf{x}-\mathbf{x}', h)\,\mathrm{d}\mathbf{x}', \tag{2}$$

where we have used integration by parts and neglected residual boundary terms. In a similar fashion, we can also obtain estimates of higher-order derivatives provided that a higher-order kernel is used.

For numerical work with SPH, the domain Ω of the fluid is subdivided into a finite set of N particles, each of mass m_b and density ρ_b (with $b = 1, 2, \ldots, N$), such that the sum of their masses equals the mass of the fluid. With this choice of the discretization, the value of $\hat{f}(\mathbf{x})$ at the location $\mathbf{x}_a$ of particle "**a**", say $f_a = \hat{f}(\mathbf{x}_a)$, is obtained by replacing Eq. (1) with the summation interpolant

$$f_a = \sum_{b=1}^{N} m_b \frac{f_b}{\rho_b} W_{ab}, \tag{3}$$

where $f_b = f(\mathbf{x}_b)$ and $W_{ab} = W(\mathbf{x}_a - \mathbf{x}_b, h)$. Note that for interpolating kernels of compact support, $W_{ab} = 0$ when $|\mathbf{x}_a - \mathbf{x}_b| \geqslant nh$, where n is some integer (usually <4) that depends on the kernel shape, and so the actual number of particles that contribute to the summation is much smaller than N. Similarly, the gradient $\nabla\hat{f}(x)$ at $\mathbf{x}_a$ is calculated by replacing Eq. (2) with the summation form

$$(\nabla f)_a = \sum_{b=1}^{N} m_b \frac{f_b}{\rho_b} \nabla_a W_{ab}, \tag{4}$$

where $\nabla_a W_{ab}$ denotes the gradient of $W(\mathbf{x}_a - \mathbf{x}_b, h)$ taken with respect to the coordinates of particle "a". However, higher accuracy for the estimate of the gradient is obtained using the alternative representation [3]

$$(\nabla f)_a = \frac{1}{\rho_a} \sum_{b=1}^{N} m_b (f_b - f_a) \nabla_a W_{ab}, \tag{5}$$

where we have made use of the identity $\rho\nabla f = \nabla(\rho f) - f\nabla\rho$. This form has the advantage that the gradient vanishes exactly when the function $f(\mathbf{x})$ is constant. A drawback of Eq. (5) is that when implementing it into the equations of motion to approximate the pressure forces, linear and angular momentum are not conserved exactly. In addition, it would be difficult to construct a consistent SPH representation for the energy equation. Therefore, it is common practice in SPH to employ the symmetrized representation

$$(\nabla f)_a = \rho_a \sum_{b=1}^{N} m_b \left(\frac{f_a}{\rho_a^2} + \frac{f_b}{\rho_b^2}\right) \nabla_a W_{ab}, \tag{6}$$

which results from rewriting $\nabla f/\rho$ according to the identity $\nabla f/\rho = \nabla(f/\rho) + (f/\rho^2)\nabla\rho$, which arises naturally from an action principle [3,35]. Similar forms to Eqs. (5) and (6) can also be derived to approximate higher-order derivatives.

2.2. SPH hydrodynamic equations

As in most SPH calculations, here the continuous density field at the location of particle "a" is evaluated via Eq. (3), with f replaced by ρ, so that

$$\rho_a = \sum_{b=1}^{N} m_b W_{ab}, \tag{7}$$

where the summation includes the contribution of particle "a" itself. Eq. (7) is used to replace the continuity equation. If this form is chosen to calculate the density, variational consistency will demand using a symmetrized SPH representation for the equations of motion and thermal energy [39].

If the pressure forces, $\nabla p/\rho$, appearing on the right-hand side of the Euler equations are approximated according to Eq. (6), we obtain the standard symmetrized SPH representation for the equations of motion

$$\frac{\mathrm{d}\mathbf{v}_a}{\mathrm{d}t} = -\sum_{b=1}^{N} m_b \left(\frac{p_a}{\rho_a^2} + \frac{p_b}{\rho_b^2} + \Pi_{ab}\right) \nabla_a W_{ab}, \tag{8}$$

where $\mathbf{v}$ is the velocity of fluid particles and p is the pressure. Here, Π_{ab} is the artificial viscous contribution to the pressure gradient (see below). An equation of state must be added to close the system of equations describing the evolution of the fluid. Here we adopt the ideal gas law written as

$$p = (\gamma - 1)\rho U, \tag{9}$$

where U denotes the specific internal energy and γ is the adiabatic index. The time rate of change of U is determined by the thermal energy equation, which is obtained from the first law of thermodynamics, $\mathrm{d}U = -p\,\mathrm{d}(1/\rho) + T\mathrm{d}s$, where T is the temperature and $\mathrm{d}s$ is the change in specific entropy, which includes all nonadiabatic effects. For isentropic flows $\mathrm{d}s = 0$ and therefore the fluid experiences only adiabatic heating and cooling. A variety of forms exists for the smoothed version of the thermal energy equation. In order to ensure variational consistency of the whole scheme, we use the symmetrized representation

$$\frac{\mathrm{d}U_a}{\mathrm{d}t} = -\frac{1}{2}\sum_{b=1}^{N} m_b \left[\left(\frac{p_a}{\rho_a^2} + \frac{p_b}{\rho_b^2} + \Pi_{ab}\right)(\mathbf{v}_b - \mathbf{v}_a) + 2H_{ab}(\mathbf{x}_b - \mathbf{x}_a)\right] \cdot \nabla_a W_{ab}, \tag{10}$$

where the term involving H_{ab} is the artificial heat conduction (see below). The discretized form of the compressional work, on the right-hand side of Eq. (10), is obtained from the identity $(p/\rho)\nabla\cdot\mathbf{v} = \nabla\cdot(p\mathbf{v}/\rho) - \mathbf{v}\cdot\nabla(p/\rho)$ after having taken the arithmetic mean of the resulting smoothed representations of both sides. In doing so, the following expression:

$$(\nabla \cdot \mathbf{v})_a = \frac{1}{\rho_a} \sum_{b=1}^{N} m_b (\mathbf{v}_b - \mathbf{v}_a) \cdot \nabla_a W_{ab}, \tag{11}$$

has been used to approximate the divergence of the velocity.

In calculations of compressible fluid flows involving the formation and propagation of shocks, an artificial viscosity term, Π_{ab}, must be added into the SPH equations to dissipate postshock oscillations in the solution and prevent particle interpenetration in high Mach number collisions. A number of expressions have been proposed for Π_{ab}. One which gives an excellent description of the flow near shocks is that proposed by Monaghan [51], where

$$\Pi_{ab} = \frac{-\alpha \bar{c}_{ab} \mu_{ab} + \beta \mu_{ab}^2}{\bar{\rho}_{ab}} \tag{12}$$

if $(\mathbf{v}_a - \mathbf{v}_b) \cdot (\mathbf{x}_a - \mathbf{x}_b) < 0$ and zero otherwise. Here

$$\mu_{ab} = \frac{(\mathbf{v}_a - \mathbf{v}_b) \cdot (\mathbf{x}_a - \mathbf{x}_b)}{h_{ab}(|\mathbf{x}_a - \mathbf{x}_b|^2/h_{ab}^2 + \eta^2)}, \tag{13}$$

$\bar{c}_{ab} = (c_a + c_b)/2$ is the average sound speed between particles a and b, $\bar{\rho}_{ab} = (\rho_a + \rho_b)/2$, and $h_{ab} = (h_a + h_b)/2$, while α and β are dimensionless constants. Typically, $\alpha \sim 1$ and $\beta \sim 2$ [46,51]. The parameter $\eta^2 \sim 0.01$ is added to the denominator of Eq. (13) to prevent numerical singularities. This choice of η^2 means that smoothing of the velocity will only take place if the particle spacing is less than $0.1h$. Implicit in the form of Eqs. (12) and (13) is that the viscosity is zero for particles moving away from each other and positive for particles approaching each other. The first term in Eq. (12) is linear in the velocity difference between interacting particles and is intended to produce a shear and bulk viscosity. The second term is quadratic and is introduced to handle high Mach number shocks. It is similar to the Von Neumann–Richtmyer viscosity employed in FD methods to smear out strong flow discontinuities. This form of the artificial viscosity is Galilean invariant and so it allows the SPH to perform well for slowly moving shocks as those involved in the Roberts [43] problem. In addition, it vanishes under solid-body rotation, conserves total linear and angular momentum, and guarantees that the entropy change due to dissipation is positive definite.

When the artificial viscosity is used in Lagrangian methods, it may produce errors in the form of excessive heating. In particular, these errors, which are commonly referred to as "wall-heating" errors after Noh [49], come into evidence in applications to infinite strength shocks, as may occur when two streams of gas collide supersonically, or when a stream of gas is brought to rest against a fixed wall as in the case of the wall shock problem. Noh [49] has shown that if an artificial heat conduction term of the form $(1/\rho)\nabla \cdot (\mathscr{H} \nabla U)$ is added to the thermal energy equation, the wall-heating errors are significantly reduced. Here we use an SPH estimate of this term given by the rule

$$H_{ab} = \frac{2\mathscr{H}_{ab}(U_a - U_b)}{\bar{\rho}_{ab} h_{ab}^2 (|\mathbf{x}_a - \mathbf{x}_b|^2/h_{ab}^2 + \eta^2)}, \tag{14}$$

where $\mathscr{H}_{ab} = (\mathscr{H}_a + \mathscr{H}_b)/2$ is the averaged artificial conduction coefficient (normalized to the density) between particles a and b, with $\mathscr{H}_a$ defined as

$$\mathscr{H}_a = g_1 h_a c_a + g_2 h_a^2 \left[|(\nabla \cdot \mathbf{v})_a| - (\nabla \cdot \mathbf{v})_a \right], \tag{15}$$

where g_1 and g_2 are constants. Typically $g_1 = g_2 \sim 0.5$. Note that although H_{ab}, enters the thermal energy equation as a heat conduction term, it is used only to control the wall-heating. It is activated only for those particles with $(\mathbf{v}_a - \mathbf{v}_b) \cdot (\mathbf{x}_a - \mathbf{x}_b) < 0$, that is, where the artificial viscosity is nonzero. Furthermore, the conduction coefficient in Eq. (15) is composed of two terms. The first one is linear in h and is a function

of the local sound speed. The second term is quadratic in h and depends on the local value of the velocity divergence. It takes a finite positive value when there is a compression ($\nabla \cdot \mathbf{v} < 0$) and vanishes otherwise. In the vicinity of a shock, this term dominates over the linear one and determines the magnitude of the conduction coefficient. This form of $\mathscr{H}$ was employed in early SPH calculations by Libersky et al. [18] and is a variant of that proposed by Monaghan [51] and Brookshaw [52], where the second term in Eq. (15) is made proportional to the absolute value of μ_{ab} as defined by Eq. (13). It is useful to mention here that the artificial heating also helps to smooth out errors in the velocity field which otherwise can induce a reduction of the artificial viscosity and hence a sharpening of the shock.

2.3. Adaptive kernel estimation

The primary motivation of this paper is to construct a shock-capturing scheme from standard SPH tools that is capable to achieve the accuracy of Riemann-based methods for most ideal gas problems. One of such SPH schemes which relies on a modified form of the dissipative terms was devised by Monaghan [34]. In this case, the SPH equations were formulated using the total energy equation instead of the thermal energy equation, as in Riemann solutions of compressible gas dynamics, and the artificial viscosity terms in the resulting SPH equations were designed in close relation to the properties of 1D solutions to the Riemann problem. Although this formulation performed quite well on the shock-tube test, it failed to follow all tests with a unique scheme. For instance, the continuity equation was used for most shock test problems, including those involving high Mach number and strong shocks, while use of the kernel summation of the density was necessary to deal with the Sjögreen [44] test, involving the propagation of two strong rarefaction waves. Also, significant wall-heating in the wall shock problem and errors in the postshock value of the density for both the blast wave and wall shock tests were clearly evident.

In this paper, we show that the accuracy of a standard SPH formulation can be significantly improved if the smoothing is based on an adaptive kernel estimation procedure like the one described by Silverman [45]. The philosophy behind this class of estimates substantially departs from that commonly used in existing adaptive SPH calculations, which are mainly based on the nearest neighbor approach [46,47]. For instance, in many applications we encounter solutions where regions of high density coexist with extended regions of low density, leading to density distributions that are characterized by rather long tails. A natural way to deal with long-tailed densities in most adaptive SPH schemes is to use a broader kernel in these regions. As a result, an observation point in the tail would have its mass smudged out over a wider range than in the main part of the distribution. This may have the disadvantage that a much larger amount of smoothing is applied to the low-density regions. In contrast, the adaptive kernel estimate of Silverman [45] copes with this problem by combining intrinsic features of both the kernel and nearest neighbor approaches in a way that the amount of smoothing applied to the data is effectively controlled. The basic idea is to construct an estimate consisting of a collection of kernels placed at the observed data points (or particles) in order to allow the bandwidth (or smoothing length) of the kernel to vary from point to point.

In the first place the method consists of deciding whether or not a particle in the sample belongs to a low-density region. This is accomplished by means of a two-stage procedure in which an initial, or *pilot*, estimate is first carried out to get a rough idea of the density. In the second stage, a pattern of bandwidths corresponding to the various observations is calculated from the pilot estimates, which is then used in the final stage to construct the adaptive estimator itself. In order to find a pilot estimate of the density, say $\tilde{\rho}_a$, we simply use the summation interpolant given by Eq. (7), with $W_{ab} = W(\mathbf{x}_a - \mathbf{x}_b, h_0)$, where h_0 is chosen by reference to an initial distribution. In practice, this value is set by the initial interparticle separation. In passing, we note that the method is insensitive to the fine detail of the pilot estimate and that there is no need for it to have any particular smoothness properties. Next, local bandwidth factors, λ_a, are defined according to the relation

$$\lambda_a = k\left(\frac{\tilde{\rho}_a}{\bar{g}}\right)^{-\epsilon}, \tag{16}$$

where $\bar{g}$ is the geometric mean of the density estimates $\tilde{\rho}_a$, given by

$$\log \bar{g} = \frac{1}{N}\sum_{b=1}^{N} \log \tilde{\rho}_b, \tag{17}$$

k is a constant scaling factor and ϵ is the so-called sensitivity parameter defined in the range $0 \leqslant \epsilon \leqslant 1$. For practical applications to compressible gas dynamics, $k \sim 1$ and $\epsilon \sim 0.5$ (see Sections 3 and 4). Finally, the width of the kernel placed at the location of particle "a" is equal to $h_a = \lambda_a h_0$. With this prescription, the adaptive kernel estimate is finally constructed by recalculating the density from Eq. (7), with $W_{ab} = W(\mathbf{x}_a - x_b, h_a)$. However, in order to ensure conservation of linear momentum, angular momentum, and total energy the actual kernel estimate that was finally employed in Eqs. (7), (8), and (10) to update the density, velocity, and thermal energy of the particles was modified by replacing h_a by the average mean [46]

$$h_{ab} = \tfrac{1}{2}(h_a + h_b), \tag{18}$$

which allows symmetrization of the kernel estimate with respect to particle pairs. Alternatively, one can use the approach suggested by Hernquist and Katz [47], where the kernel itself is symmetrized according to the expression

$$W_{ab} = \tfrac{1}{2}\big[W(\mathbf{x}_a - \mathbf{x}_b, h_a) + W(\mathbf{x}_a - \mathbf{x}_b, h_b)\big]. \tag{19}$$

According to Eq. (16), the local bandwidth factors, λ_a, will be more sensitive to variations in the pilot density for higher values of the power ϵ, implying a greater difference between the bandwidths, h_a, in different parts of the sample. A value of $\epsilon = 0$ will reduce the method back to the fixed width kernel approach provided that $k = 1$ in Eq. (16). Furthermore, with the λ_a calculated as in Eqs. (16) and (17), the h_a's effectively control the scale of the smoothing applied to the data. In this way, using Eq. (7) to define the pilot estimate makes it to be sensitive to the same sort of scale as the final adaptive estimate. While this procedure gives better results, it has the disadvantage of calculating twice the summation interpolant per timestep. However, provided that the kernel function W is nonnegative, the adaptive kernel estimate will be a *bonafide* probability density. It will not suffer from the excessively heavy tails as the nearest neighbor method does in the sense that the minimum necessary smoothing will be applied to regions of low density. Although in general this aspect improves the accuracy of the SPH method, it becomes particularly important for distributions involving sudden jumps in the variables as may be the case of phenomena involving strong shocks.

The use of a variable smoothing length would certainly require the inclusion of additional terms on the right-hand side of Eqs. (8) and (10). These terms, called the ∇h correction terms, contain the contribution of the $\partial W/\partial h$ derivatives and their form was first derived by Nelson and Papaloizou [54] for the case of smoothing lengths symmetrized as in Eq. (18). The same authors [55] have also derived the corresponding form of the ∇h terms for the kernel symmetrization given by Eq. (19). The need for such terms was first illustrated by Hernquist [53], who showed that in the simulation of a head-on collision between two polytropic gas spheres, errors of about 10% can occur in the conservation of either energy or entropy, depending on whether the energy or entropy equations are integrated. Nelson and Papaloizou [55] designed a number of tests, including the shock tube problem, the gravitational collapse of a cold gas sphere, and the head-on collision of two polytropes, to study the effects of these corrections on SPH simulations. They found that for the first two test calculations the inclusion of the ∇h terms does not alter the ability of SPH to reproduce, with reasonable accuracy, the qualitative and quantitative features of the solution. In the third test, however, where the conservation properties are more critical, the inclusion of the ∇h terms led to a dramatic improvement in the conservation of energy and entropy regardless on whether the energy or entropy equa-

tion was integrated. From their analysis, it then follows that the influence of the ∇h terms on SPH simulations may be relevant under rather special circumstances. More recently, Alimi et al. [56] considered the effects of including the ∇h terms in cosmological simulations. In particular, they found that when the ∇h terms are neglected, the density peaks associated to shock fronts are overestimated as a consequence of the resulting erroneous smaller entropy in these regions. However, the qualitative features of the solution were reproduced in any case. Based on the results reported by Nelson and Papaloizou [55] on the shock tube problem, where identical solutions were obtained independently on whether the ∇h terms are included or neglected, and considering that these terms seem to be relevant for a restricted class of problems we have preferred to neglect their inclusion for the calculations of this paper.

The adaptive kernel estimation procedure proposed here can be applied to a variety of other problems of interest, including systems with components of elastic and inelastic materials such as deformation of elastic bodies [20,38], fracture of brittle materials [22,24,25,28], and tracking of debris clouds produced by ballistic impacts on elastic plastic solids [18,21,23,26,27]. Most of these problems require the inclusion of the entire stress tensor in Eqs. (8) and (19), as in simulations of viscous fluids, and a natural treatment of voids, as in simulations of dynamic brittle fracture, where existing flaws under tension may eventually evolve into cracks that must be represented numerically. In particular, the SPH formalism has certain advantages over other methods for modeling strong material deformation and fracture. Once the damage is calculated and the material properties degraded, SPH allows for the natural insertion of voids, and unlike conventional Lagrangian techniques, it avoids mesh tangling and is therefore much more robust in its treatment of problems with large material distortions. The differential equations describing the dynamics of deformable solids are identical in form to those for a viscous fluid, except that in the former case the anisotropic part of the stress tensor (the deviatoric stress) is determined from an extra differential equation for its time rate of change, which must be included in order to follow the material response to deformations due to strain and rotations [18]. The symmetrized SPH representations of the momentum and internal energy equation have a form similar to those given by Eqs. (8) and (10), with the pressure replaced by the components of the stress tensor. The time rate of change of the deviatoric stress admits an SPH representation as given by Eq. (44) of Libersky et al. [18]. As in Eqs. (8) and (10), all derivatives in the source part of the equations will appear in terms of the derivatives of the kernel and therefore the adaptive kernel estimation proposed here can be applied in the same manner as for the fluid-dynamic equations. This procedure can be employed to describe strong density discontinuities in solids, as may be the case of strong shocks across material interfaces or the occurrence of cracks in brittle fracture problems, provided that some adequate boundary condition treatment is employed. In particular, the kernel estimation procedure given by Eqs. (16) and (17) can be applied in a straightforward manner with the method of ghost particles described by Randies and Libersky [31] to deal with irregular and deformable sharp boundaries or material interfaces. In the same way, the kernel estimation procedure presents no problems when used in conjunction with the more conventional method of image particles [4] to model regular rigid boundaries.

2.4. Kernel functions

In the calculations of this paper we use both the Gaussian kernel and the cubic B-spline function of Monaghan and Lattanzio [57]. These are among the most widely used interpolation kernels in current SPH simulations. In particular, the Gaussian kernel is modified for compact support according to the prescription

$$W(q,h) = \frac{1}{\pi^{\nu/2}h^{\nu}} \begin{cases} \mathrm{e}^{-q^2} & \text{if } 0 \leqslant q \leqslant 3, \\ 0 & \text{if } q > 3, \end{cases} \tag{20}$$

so that the kernel goes to zero at a distance $3h$ from its peak. This provides a limit on the number of neighbor particles. Here $q = |x - x'|/h$ and ν is the number of dimensions. This kernel defines a sequence which

mimics a δ-function in the limit $h \to 0$ and is infinitely differentiable. As a further choice, we also use the cubic B-spline kernel [57]

$$W(q,h) = \frac{\sigma}{h^{\nu}} \begin{cases} \frac{2}{3} - q^2 + \frac{1}{2}q^3 & \text{if } 0 \leqslant q < 1, \\ \frac{1}{6}(2-q)^3 & \text{if } 1 \leqslant q < 2, \\ 0 & \text{if } q > 2, \end{cases} \tag{21}$$

where all parameters have the same meaning as before and σ is a normalization constant equal to 1 and $15/7\pi$ in one and two dimensions, respectively. With this form of the kernel, the particle interactions are exactly zero at distances from the peak of the distribution greater than $2h$. In addition, the second derivatives are continuous and the dominant error term in the integral interpolants is $O(h^2)$. In particular, we find that the results are essentially independent of whether Eq. (20) or (21) is used.

3. One-dimensional numerical tests

In order to assess the capabilities of the present method we test it against a suite of well-known 1D shock problems for which the hydrodynamical states are either uniform, as in the standard Riemann shock-tube problem [41], or spatially varying, as in the impulsive load problem of Zel'dovich and Raizer [48]. In all cases, the analytical solution is available and so we can provide a direct measure of the accuracy of the numerical results.

3.1. The shock tube

As a first numerical experiment we consider the classical shock-tube problem [41]. In this test, a diaphragm is placed at $x = 0$ which separates two regions of constant density and pressure. The initial conditions consist of gas at rest with $\gamma = 1.4$ ($\rho_{\rm L} = 1$, $p_{\rm L} = 1$, $U_{\rm L} = 2.5$) for the left state ($x < 0$), and ($\rho_{\rm R} = 0.25$, $p_{\rm R} = 0.1795$, $U_{\rm R} = 1.795$) for the right state ($x > 0$). Note that the same initial parameters were used by Nelson and Papaloizou [55] and Cha and Whitworth [36]. At $t > 0$, the diaphragm is broken and the initial discontinuity splits up into three regions. The first one consists of a rarefaction wave moving to the left within which the fluid variables are continuous. To the right of the rarefaction tail, there is a second region which extends up to the location of the contact discontinuity, which gives the position that an element of fluid initially at $x = 0$ has reached by time t. Across the contact discontinuity the velocity and pressure are continuous, while the density and thermal energy are discontinuous. To the right of the contact surface there is a postshock region bordered by a shock wave moving to the right. With the above initial conditions, the Mach number of the resulting shock is 1.481.

As in Monaghan [34], we started the calculation by smoothing all initially discontinuous quantities according to the prescription

$$A = \frac{A_{\rm L} + A_{\rm R} {\rm e}^{x/d}}{1 + {\rm e}^{x/d}}, \tag{22}$$

where A may be either ρ, p, or U. Here $A_{\rm L}$ and $A_{\rm R}$ refer to the left and right states, respectively, and d is half the largest initial particle separation at the location $x = 0$ of the initial discontinuity. A total number of 3000 particles were used along the interval $-0.6 \leqslant x \leqslant 0.6$, of which 600 equidistant particles were placed to the right of the origin, yielding an initial spacing $\Delta x_{\rm R} = 0.001$ for $x > 0$. The remaining 2400 particles were placed to the left of $x = 0$ according to the rule

$$x_{a+1} = x_{a-1} + \frac{2\rho_{\rm R}\Delta x_{\rm R}}{\rho_a}, \tag{23}$$

where ρ_R denotes the gas density to the far right of the origin. For this test case we chose $\alpha = \beta = 1$ in Eq. (12) for the artificial viscosity, $g_1 = 0.02$ and $g_2 = 0.4$ in Eq. (15) for the artificial heat conduction, and $k = 0.7$ and $\epsilon = 0.4$ in Eq. (16) for the calculation of the local bandwidth factors λ_a. In addition, the timestep was fixed to $\Delta t = 3.0 \times 10^{-4}$ and the initial value of the smoothing length was set to twice the spacing Δx_R.

The results for this test are shown in Fig. 1 at $t = 0.15$. We may see that the numerically calculated solution (dots) reproduces the exact one (solid line) with very good accuracy. At this time, the contact surface is at $x = 0.101$, while the shock is at $x = 0.223$. The density behind the contact discontinuity is 0.5463 (exact value 0.5467) and that behind the shock is 0.4576 (exact value 0.4573). These values imply relative errors of about $7.0 \times 10^{-2}\%$ in the density. The postshock pressure is 0.4296 (exact value 0.4293). Starting from the location of the rarefaction tail (at $x = -0.0553$), the pressure remains constant up to the shock position. Note that only an unperceivable wiggle is present around the contact discontinuity. This very small pressure wiggling is a reflection of the small spike in the thermal energy distribution just ahead of the contact surface. Both features essentially disappear when the value of the constant g_1 entering in the linear term of Eq. (15) is raised to about 0.07. However, as a result of the increased linear artificial heating, the numerical description of the contact surface will not be as sharp as that displayed in the density- and energy-distance plots of Fig. 1. The postshock value of the thermal energy is 2.3474 compared to the exact value of 2.3470, while behind the contact discontinuity the numerically calculated value is 1.9629 (exact value 1.9635). In addition, from the velocity-distance plot we may see that the numerical solution is free of oscillations behind the shock, with a postshock velocity of 0.6733 in contrast to the analytical value of 0.6731. Also note that the rarefaction wave and the shock discontinuity are very well reproduced.

We may also see from the density- and energy-distance plots that both the shock and contact discontinuity have almost identical resolution. This is one important aspect of the adaptive kernel estimation method described in Section 2.3. In particular, Fig. 2 depicts the dependence of h_a, normalized to the initial value

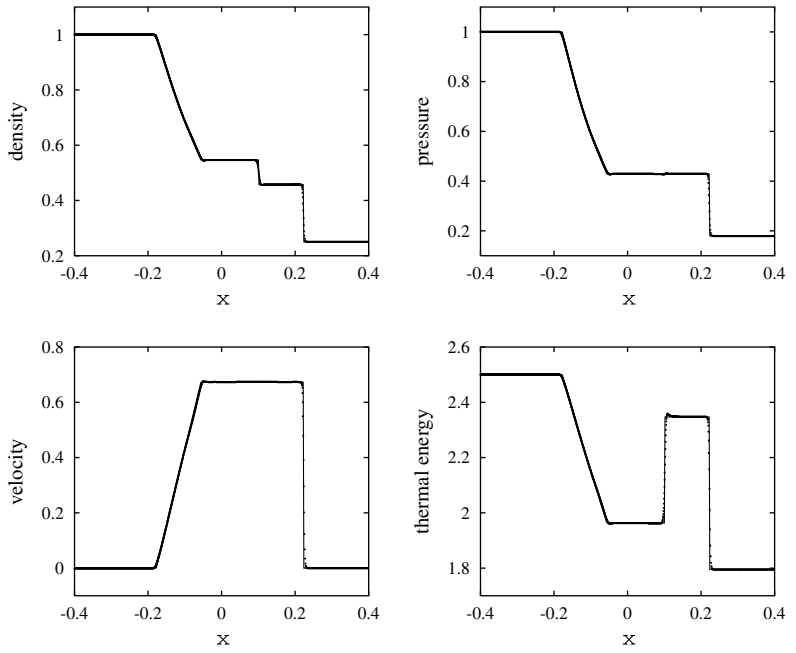

Fig. 1. Results for the Sod's shock-tube problem at $t = 0.15$. The gas to the right of the initial discontinuity is represented by 600 particles of equal mass, yielding a uniform spacing $\Delta x_R = 0.001$. The numerically calculated solution (dots) reproduces the exact one (solid line) with very good accuracy.

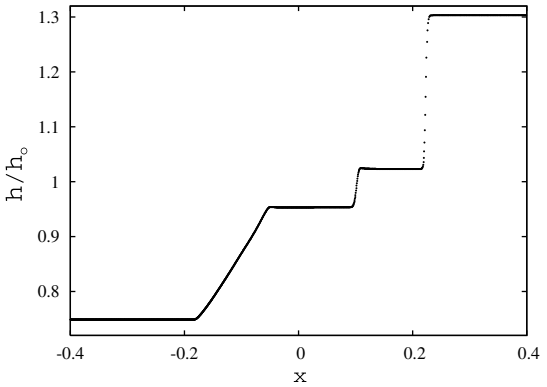

Fig. 2. Spatial dependence of the particle's smoothing length h, normalized to the initial value $h_0 = 2\Delta x_R$, at time $t = 0.15$ for the same shock-tube calculation of Fig. 1. The sharp variations of h at the location of the contact surface and shock wave clearly show the adaptive nature of the calculation.

$h_0 = 2\Delta x_R$, with distance at $t = 0.15$. The sharp variations of h_a at both the shock and contact surface clearly show the adaptive nature of the smoothing length as determined from Eqs. (16) and (17). Similar results were obtained when varying the parameters k and ϵ within the intervals $(0.9, 0.65)$ and $(0.4, 0.55)$, respectively. However, we found that the best compromise between getting postshock profiles free of oscillations and sufficiently sharp jumps of the hydrodynamical variables across the physical discontinuities was to choose a sensitivity parameter ϵ around 0.4. In particular, values of ϵ less than 0.4 result in a broader description of the jumps due to the increased smoothing in regions of lower density.

3.2. The blast wave

We now test the method on the blast wave problem introduced by Woodward and Colella [42]. This test is a modified version of the shock-tube problem and involves extremely supersonic flows. The initial conditions consist of an ideal gas at rest with $\gamma = 1.4$ and left ($x < 0$) and right ($x > 0$) states given by $\rho_L = 1$, $p_L = 1000$, $U_L = 2500$ and $\rho_R = 1$, $p_R = 0.01$, $U_R = 0.025$, respectively. In contrast to the shock-tube test, the initial pressure of the gas on the left-hand side is 10^5 times that of the right-hand side. This results in an approximately Mach 200 shock. In particular, the blast wave problem is known to be a severe test because the velocity of the contact discontinuity (exact value 19.60 at $t = 0.0075$) is close to the shock speed (exact value 23.52 at $t = 0.0075$), producing a sharp spike in the density variation just behind the shock. For this calculation we used 1000 equidistant particles on each side of the initial discontinuity to cover the interval $-1 \leq x \leq 1$, yielding a uniform spacing $\Delta x = 0.001$. The initial smoothing length was set to $h_0 = 1.5\Delta x$ and the calculation was carried out with a constant timestep ($\Delta t = 5 \times 10^{-6}$) and $\alpha = \beta = 1$, $g_1 = 0.2$, $g_2 = 0.4$, $k = 1$, and $\epsilon = 0.5$. For this test no use of Eq. (22) was made to smooth the initially discontinuous physical quantities.

Fig. 3 shows the numerical results (dots) as compared with the exact solution (solid line) at $t = 0.0075$, when the shock is at $x = 0.1764$. The density and thermal energy variations reproduce very well the analytical solution except at the contact discontinuity, where the method yields a smooth distribution of the density and thermal energy. Also, the pressure and velocity distributions show a small wiggle at the contact surface. When a value of g_1 much less than 0.2 is used, the contact discontinuity becomes much sharper at the expense of a slight increase of the wiggling amplitude. Conversely, higher values of g_1 yield wiggles of much smaller amplitude and broader contact surfaces. For the same test, the calculations of Monaghan [34] gave a better description of the contact discontinuity towards the upper part of the density spike. However,

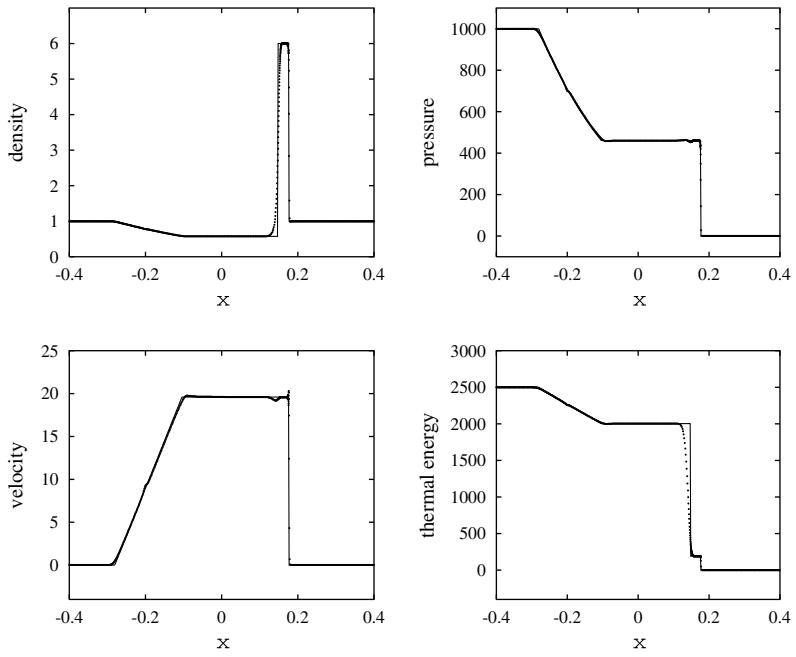

Fig. 3. Results for the one-dimensional blast wave problem at $t = 0.0075$. The pressure to the left of the initial discontinuity is 10^5 times that to the right, resulting in an approximately Mach 200 shock. We used 1000 equidistant particles of equal mass on each side of the initial interface ($\Delta x = 0.001$). The numerical solution (dots) compares very well with the exact one (solid line), except at the contact surface where the method produces a smooth profile.

in his case the density spike was overestimated by about 10%. By comparison, our calculations yield a postshock density of 5.998 (exact value 6.0) for most of the upper plateau. Note that for all quantities the rarefaction and the shock waves are also very well described, except for a small wiggling at $x = -0.2$. We may also note the small upward spike in the velocity at the shock position. In particular, the postshock values of the pressure, velocity, and thermal energy are 459.68 (exact value 460.89), 19.71 (exact value 19.60), and 191.58 (exact value 192.06), respectively, which correspond to relative errors of better than 0.3% in the pressure and thermal energy and of about 0.6% in the velocity. In passing, we note that the solutions shown in Fig. 3 strongly resemble those reported by Inutsuka [35] (see his Figs. 7 and 8) for a similar test but with a Mach 10^5 shock, using an SPH method that completely relies on solution to the Riemann problem.

3.3. The wall shock

We now consider the problem of a configuration consisting of a cold stream of gas flowing towards a solid wall. As the gas hits the wall, a shock front forms which then travels upstream against the incoming gas, producing a hot, dense postshock region of zero velocity. This problem is the equivalent of a system consisting of two cold streams of gas, one in front of the other, travelling with oppositely directed velocities. We take the wall as the $x = 0$ plane and define the left state ($x < 0$) as the exact reflection of the right one ($x > 0$). We use the same initial parameters of Monaghan [34], namely $\rho_L = 1$, $v_L = 1$, $U_L = 10^{-6}$ for $x < 0$ and $\rho_R = 1$, $v_R = -1$, $U_R = 10^{-6}$ for $x > 0$, with $\gamma = 1.4$. Note that only the velocity is discontinuous at $x = 0$. We used 800 equidistant particles in the interval $-0.1 \leqslant x \leqslant 0.1$ to represent the two gas streams, resulting in a uniform spacing $\Delta x = 0.0005$. The initial smoothing length was chosen to be equal to the interparticle distance and a constant timestep of 1.0×10^{-6} was used throughout the calculation, with

$\alpha = \beta = 1$, $g_1 = 0.5$, $g_2 = 1.0$, $k = 0.7$, and $\epsilon = 0.4$. Values of the estimation parameters within the intervals $1.0 \leqslant k \leqslant 0.7$ and $0.4 \leqslant \epsilon \leqslant 0.6$ were seen to produce similar results.

The results for this test case are shown in Fig. 4 at $t = 0.1$. The position of the shock at this time ($x = 0.02$) is very well reproduced. The worst relative errors in the postshock values of the density, pressure, and thermal energy are always better than 0.3%. The velocity is obtained accurately with a sharp shock and negligible ripples. The postshock velocity is always less than 10^{-4}, except close to the shock where it degrades to better than 10^{-2}. For the same test Monaghan [34] found a postshock density value which was 10% in excess of the exact solution along with a pronounced downward spike at the location of the wall due to significant wall-heating error in his calculation. As a result of this, a small upward spike was also present in the postshock thermal energy distribution at $x = 0$. The results of Fig. 4 shows that the postshock plateaus are very well reproduced and that they are free of the unphysical spikes caused by the wall-heating error, implying that the present method is also able to handle shocks of very high strength.

3.4. The Roberts problem

In a well-known paper [43], Roberts found that for a nearly stationary shock, there is a significant error produced when using Godunov-type methods based on flux difference splitting algorithms. The error appears in the form of a long wavelength noise, which is generated in the discrete shock transition layer and is transported downstream. This error is a consequence of the nonlinear character of the hydrodynamical equations and cannot be damped out by the inherent dissipation of the Godunov schemes. A discussion on the nature of this error along with a heuristic explanation of it was provided by Colella and Woodward [58] in the context of their PPM method. In particular, they constructed

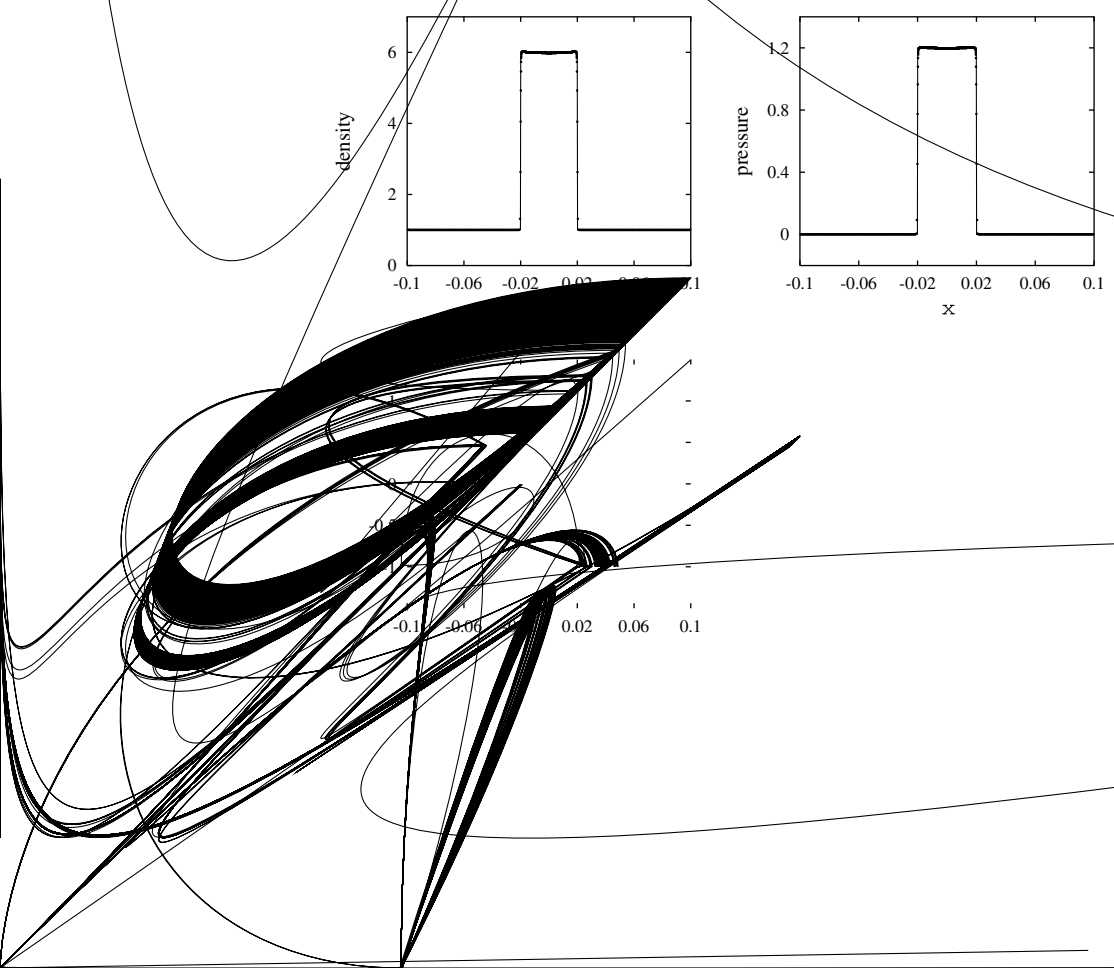

additional numerical dissipation terms to minimize the oscillations. However, as pointed out by Monaghan [34], SPH presents no difficulties on this test problem because of its Galilean-invariant nature.

The Roberts problem consists of a Mach 3 shock wave moving slowly from left to right in a $\gamma = 1.4$ gas. The postshock state is given by $\rho_L = 3.86$, $v_L = -0.81$, $p_L = 10.33$, while the preshock state is $\rho_R = 1$, $v_R = -3.44$, $p_R = 1$. These initial conditions are the same employed by Xu et al. [59] and Monaghan [34]. With this choice of the initial parameters, the shock speed is $v_{sh} \approx 0.11$ and its location at time t is given by $x = x_0 + v_{sh}t$. Here we take the plane $x_0 = 0$ as the starting shock. In order to speed up the calculation we add a constant velocity ($v = 0.42$) to the values of v_L and v_R. In doing so the position of the shock at any time ($t > 0$) is just $x = (v_{sh} + v)t$. After a sufficiently long time, an accurate description of the shock will demand using a relatively large number of initial particles. As shown in Fig. 5, sharp enough shock profiles are obtained by placing 7500 uniformly spaced particles to the left of the shock (covering the interval $-4.8 \leqslant x \leqslant 0$) and 2500 particles to the right (covering the interval $0 < x \leqslant 8$). With this resolution $\Delta x_L = 0.00064$ and $\Delta x_R = 0.0032$. The calculation was performed with a constant timestep $\Delta t = 1.0 \times 10^{-4}$, $h_0 = \Delta x_R$, and the same parameters as for the wall shock test, except that $k = 1$ and $\epsilon = 0.5$. Fig. 5 depicts the shock structure at $t = 1.5$ in the evolution. At this time the shock is located at $x = 0.794$ and the results are comparable to those reported by Monaghan [34] and Xu et al. [59]. The density and pressure jumps are very well resolved and the postshock profiles are free of the long wavelength oscillations reported by Roberts [43]. Similarly, well-resolved shock profiles were also obtained for the velocity and thermal energy.

3.5. The Sjögreen problem

A further test model deals with a Riemann problem whose initial data are given by $\rho_L = 1$, $v_L = -2$, $p_L = 0.4$, $U_L = 1$ for the left state ($x < 0$) and $\rho_R = 1$, $v_R = 2$, $p_R = 0.4$, $U_R = 1$ for the right state ($x > 0$). Here $\gamma = 1.4$. One state is the mirror of the other and so reflected boundary conditions can be used at $x = 0$. This problem was discussed by Einfeldt et al. [44] and its solution consists of two strong rarefaction waves, one travelling to the left and the other to the right. Since the fluid flow is directed away from the origin, a region of very low density and pressure forms within the rarefactions. For the above initial state, the Mach number M (≈ 2.67) $< 2/(\gamma - 1)$ and therefore no vacuum will occur in the solution. In addition, since

$$M < \sqrt{\frac{2}{\gamma(3-\gamma)}}, \tag{24}$$

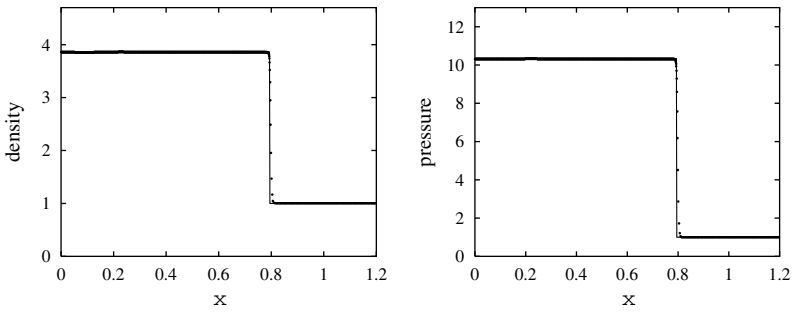

Fig. 5. Density and pressure profiles for the Roberts problem at $t = 1.5$ when the shock has travelled a distance $x = 0.794$ from the origin ($x = 0$). The numerical solution (dots) is compared with the exact shock structure (solid line). Similarly, well-resolved shock profiles were also obtained for the velocity and thermal energy.

the solution is positively conservative (that is the density and thermal energy are positive) but not linearizable. Most Godunov-type schemes whose interface fluxes are derived from a linearized Riemann solution are not positively conservative and so they fail on this test problem [44].

For this calculation we used 800 uniformly distributed particles covering the spatial range $-1 \leqslant x \leqslant 1$, with 400 particles placed on each side of $x = 0$. This yields an interparticle distance $\Delta x = 0.0025$. Good results were obtained by first smoothing the initial density through the use of Eq. (7), with $h_0 = 2.5\Delta x$, and then recalculating the smoothing length according to $h_{0,a} = 2m_a/\rho_a$, where m_a is the mass of particle "a" and ρ_a its initial smoothed density. The calculation was performed with $\alpha = \beta = 1$, $g_1 = 0.1$, $g_2 = 1.0$, $k = 0.5$, $\epsilon = 0.1$, and a constant timestep $\Delta t = 1.0 \times 10^{-3}$. Since no shocks are involved in this test, identical results were obtained by switching off the artificial viscosity ($\alpha = \beta = 0$) and artificial heat conduction ($g_1 = g_2 = 0$) terms in Eqs. (8) and (10). Fig. 6 shows the numerical solution (dots) as compared to the exact one (solid line) at $t = 0.3$. The characteristic U profiles for the density and pressure are accurately reproduced along with the condition that these quantities remain positive. The worst relative errors occur in the central part, where the density and pressure of the two particles closest to $x = 0$ are 0.022 (exact value 0.015) and 0.0024 (exact value 0.0011), respectively. The position of the rarefaction heads is also well reproduced by the numerical solution. The dependence of the linear momentum ($\rho \mathbf{v}$) with distance also compares satisfactorily with the exact behavior. Higher accuracy on this test problem near $x = 0$ can be obtained by increasing the initial number of particles. In particular, the velocity is by far more sensitive to the initially allowed resolution than all other quantities. This can be readily inferred from the resulting velocity profile, where the slopes of the two-rarefaction straight lines and the extension of the joining plateau differ from the exact solution. Similar results for the velocity were also obtained by Einfeldt et al. [44] using a conservative

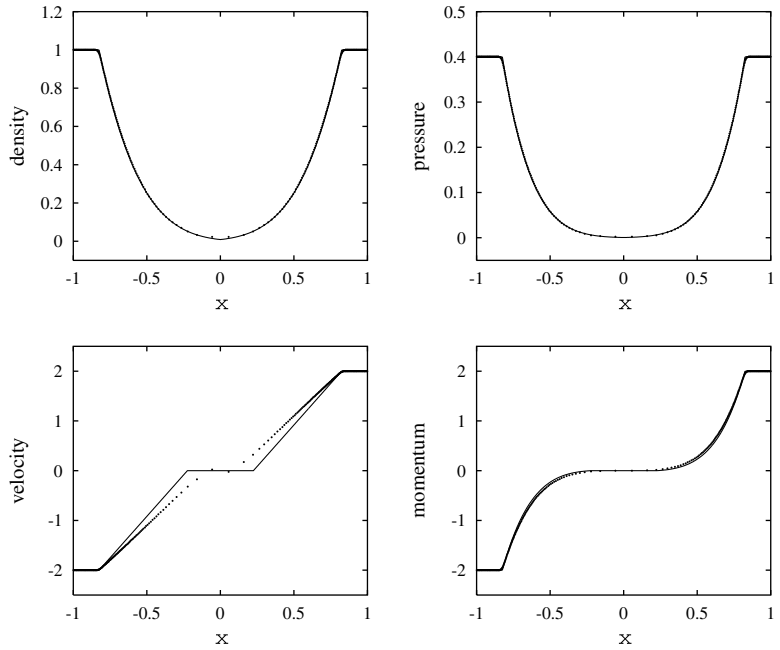

Fig. 6. Numerical results (dots) for the Sjögreen problem in which two high-speed, strong rarefaction waves move apart from each other, as compared with the exact solution (solid line). We used 800 particles of equal mass in the interval $-1 \leqslant x \leqslant 1$, yielding a uniform spacing $\Delta x = 0.0025$. The characteristic U shape of the density and pressure arising from the rarefactions is accurately reproduced by the numerical solution. A much better agreement of the velocity with the exact solution can be obtained with finer resolution.

differencing Godunov method based on the original Roe scheme and by Monaghan [34] and Cha and Whitworth [36] using their shock-capturing SPH schemes.

3.6. Impulsive load in an inhomogeneous atmosphere

In contrast to all previous cases, we now test the response of the method for a 1D model problem in which the initial hydrodynamical state is spatially varying. In particular, we consider the self-similar motion of a shock wave, induced by a strong explosion, in the direction of increasing density as described by Zel'dovich and Raizer [48]. The unperturbed state consists of an inhomogeneous gas at rest with zero pressure and density given by the exponential law

$$\rho(x) = \rho_0 \exp\left(\frac{x}{\Delta}\right), \tag{25}$$

where Δ is a constant and ρ_0 is a reference density. Let an impulsive load be applied at some initial time t_0 somewhere in the region of low density. As a result, a shock wave arises which then travels through the gas in the direction of increasing density, while the heated gas expands in the opposite direction. If we define x_0 as the location of the shock front at time t_0, a Riemann problem can be constructed with the left ($x \leqslant x_0$) and right ($x > x_0$) states given by

$$\begin{aligned}
\rho_{\mathrm{L}}(x,t_0) &= \rho_0\left(\frac{\gamma+1}{\gamma-1}\right)(1+2\xi_0)^{-5/2},\\
v_{\mathrm{L}}(x,t_0) &= \eta\left(\frac{2}{\gamma+1}\right)\left(\frac{\Delta}{t_0}\right)(1-\xi_0),\\
U_{\mathrm{L}}(x,t_0) &= 2\left(\frac{\eta}{\gamma+1}\right)^2\left(\frac{\Delta}{t_0}\right)^2(1+2\xi_0),
\end{aligned} \tag{26}$$

and

$$\begin{aligned}
\rho_{\mathrm{R}}(x,t_0) &= \rho_0\exp(-\xi_0),\\
v_{\mathrm{R}}(x,t_0) &= 0,\\
U_{\mathrm{R}}(x,t_0) &= 0,
\end{aligned} \tag{27}$$

respectively, where Δ is the characteristic scale of the impulsive width, $\xi_0 = (x_0 - x)/\Delta$ is a dimensionless distance, and η is a numerical coefficient that depends only on the specific heat ratio γ.

An exact solution for $t > t_0$ exists when $\gamma = 2$ (for which $\eta = 3/2$) and is given by [48]

$$\begin{aligned}
\rho_{\mathrm{L}}(x,t) &= 3\rho(x_{\mathrm{f}})(1+2\xi)^{-5/2},\\
v_{\mathrm{L}}(x,t) &= \frac{\Delta(1-\xi)}{t},\\
U_{\mathrm{L}}(x,t) &= \frac{1}{2}\left(\frac{\Delta}{t}\right)^2(1+2\xi),
\end{aligned} \tag{28}$$

for $x \leqslant x_{\mathrm{f}}(t)$, and

$$\begin{aligned}
\rho_{\mathrm{R}}(x,t) &= \rho_0\exp(-\xi_0),\\
v_{\mathrm{R}}(x,t) &= 0,\\
U_{\mathrm{R}}(x,t) &= 0,
\end{aligned} \tag{29}$$

for $x > x_{\mathrm{f}}(t)$. Here $x_{\mathrm{f}}(t) = x_0 + 1.5\Delta\ln t$ is the coordinate of the shock front, which varies logarithmically with time, and $\xi = [x_{\mathrm{f}}(t) - x]/\Delta$. The shock velocity decreases with time and is given by $v_{sh} = 1.5\Delta/t$. As

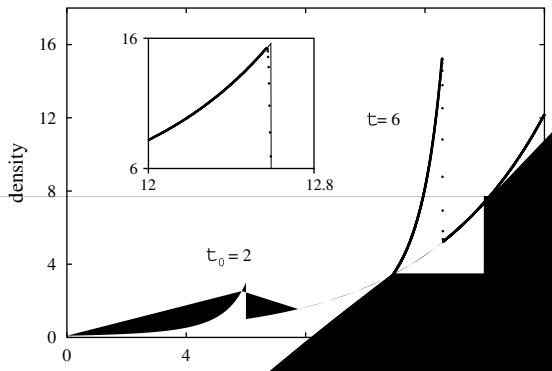

Fig. 7. Initial state at $t_0 = 2$ (dashed line) and exact solution
inhomogeneous gas. The dots represent the numerical
postshock profile. The density peak is underestimated
of the density is reproduced very well.

the starting point of the calculation we u
[60], and compare the SPH solution with
posite Lagrangian FD code solution. Fig.
(dashed line) and at $t = 6$ (solid line) whe

This test calculation was carried ou
$0 \leqslant x \leqslant 6$ and 2250 particles for $6 <$
$g_1 = g_2 = 1$, $k = 1$, $\epsilon = 0.5$, $\Delta t = 1.0 \times$
at $t = 6$. The small inset box displa
2.34% relative error in the peak v
ical solution overlaps the exact
happening at $x = 12.57$ (exact
dependence of the pressure,

4. Two-dimensional tests

The extension of t
[50] point explosion
compared with th

4.1. The Noh

The unif h [49]
turing co form de
ally inw ength is
broug ditions fo
unit $\rho^0 = 1,$ $U(r, 0) =$
cyli he analytica shock
v preshock value $= 16,$

$[\rho^- = \rho^0(1 + t/r)$, $v^- = v^0 = -1$, $U^- = U^0 = 0$, $p^- = p^0 = 0]$, respectively. At the shock position ($r_{sh} = t/3$), the value of the preshock density is exactly 4. This value is independent of time and hence leads to the constant postshock profiles given above.

For this test, we choose the (r, ϕ)-plane to represent the flow and distribute the particles along the perimeter of n concentric circles around the axis of symmetry. The radial separation between consecutive circles is $\Delta r = 1/n$ such that $R = n\Delta r = 1$ is the radius of the outermost circle, where the boundary condition $v(R = 1, t) = -1$ is applied. The number of particles per circle increases with increasing radius according to $N_j = 4j$, where $j = 1, 2, \ldots, n$. Therefore, the angular interparticle separation decreases with increasing radius and is given by $\Delta\phi_j = \pi/(2j)$. With this choice, the innermost circle ($j = 1$) will always be composed of only four particles, each of mass $m_1 = \pi(\Delta r)^2\rho^0/4$, separated in angle by $\pi/2$. Accordingly, the mass of all particles belonging to the jth circle is given by

$$m_j = \frac{(2j-1)}{j} m_1, \tag{30}$$

for $j = 2, 3, \ldots, n$. In this way, the increase of the particle mass with radius is limited to the small range $1 \leqslant m_n/m_1 \leqslant (2n-1)/n$. Two independent calculations were performed with 29,040 and 61,600 particles, corresponding to $n = 120$ ($\Delta r \approx 0.0083$) and 175 ($\Delta r \approx 0.0057$) concentric circles, respectively. As for the wall shock test, we chose $\alpha = \beta = 1$, $g_1 = 0.5$, and $g_2 = 1$. For the density estimation parameters we used $k = 0.9$ and $\epsilon = 0.4$ along with $h_0 = \Delta r$ and a constant timestep $\Delta t = 5.0 \times 10^{-4}$.

Early SPH calculations of the cylindrical Noh's shock problem were carried out by Libersky et al. [18], who used comparable spatial resolution (15,482 and 60,000 particles) and the same form of the artificial viscosity and heating given by Eqs. (12)–(15). A comparison with their results is therefore useful to provide further evidence of the increased resolving power of the adaptive kernel estimation. The outcome of the evolution is shown in Fig. 8, where the density and thermal energy are plotted as functions of the radius for each particle at $t = 0.6$. The solid line depicts the exact solution, while the asterisks and open circles correspond to the numerical profiles for the low- (29,040 particles) and high-resolution (61,600 particles) runs. Note that all SPH particles fall on one curve, implying that symmetry is achieved by the calculations. A surface density plot is also shown in Fig. 9 at $t = 0.6$ for the high-resolution case. As it is well-known, the presence of wall-heating results in an extreme dip in the density with a corresponding overshoot in the thermal energy at the origin ($r = 0$). These features persist even working with finer resolution (see Fig. 1 of [18]). For both resolutions, the results of Fig. 8 are superior to those reported by Libersky et al. [18], where the presence of an extreme density dip close to the axis is evident and the shock is poorly resolved. Although a density dip is still present in Fig. 8 ($\rho \approx 15.29$ and 15.39 for

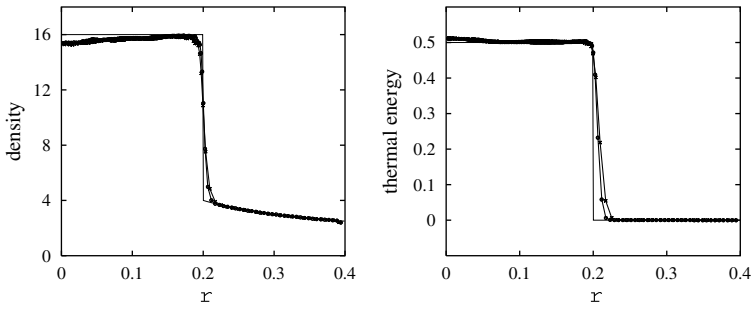

Fig. 8. Numerical profiles calculated with different initial resolutions (asterisks: 29,040 particles; open circles: 61,600 particles) at $t = 0.6$ for the two-dimensional cylindrical Noh's shock problem. The exact solution (solid line) is also plotted. Only a small density dip and a small thermal energy overshoot occur at the origin ($r = 0$).

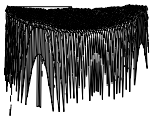

the low- and high-resolution runs; exact value 16), it is much smaller than that observed with other codes, including the FD composite scheme of Shashkov and Wendroff [60] at comparable spatial resolution (see their Fig. 4(b)). It follows from Fig. 8 that the high-resolution calculation produces similar post-shock profiles and a slightly sharper shock compared to the low-resolution run. Because of the coarse radial resolution allowed here, the description of the shock is not as sharp as those seen in the 1D model calculations of Section 3. For this 2D problem, we therefore expect to see the solution improve with the use of finer radial resolution.

4.2. The Sedov problem

As a final test calculation, we consider the Sedov point explosion problem in cylindrical geometry, which involves the self-similar propagation of a cylindrical blast wave from a δ-function initial pressure perturbation in a homogeneous medium at rest. The analytical solution for this problem was originally derived by Sedov [50], under the assumption that the atmospheric pressure relative to that inside the explosion is negligible.

The point explosion is assumed to occur at the origin ($r = 0$) at time $t = 0$. In the self-similar cylindrical blast wave that develops at $t > 0$, the density, velocity, and pressure are all functions of the similarity variable $\xi = r/R(t)$, where

$$R(t) = \beta^{-1}\left(\frac{et^2}{\rho_0}\right)^{1/4} \tag{31}$$

is the radius of the shock. Hence, the surface $\xi = 1$ represents the outgoing shock wave. In Eq. (31), ρ_0 is the density of the homogeneous medium, e is the quantity of energy deposited at $r = 0$, and β is a constant of order unity to be determined. At any time $t > 0$, the state behind the outgoing shock ($0 \leqslant \xi \leqslant 1$) is determined by the self-similar solution

$$\begin{aligned} \rho_{\mathrm{L}}(r,t) &= \rho_0 G(\xi), \\ v_{\mathrm{L}}(r,t) &= \frac{r}{2t} V(\xi), \\ c_{\mathrm{L}}^2(r,t) &= \frac{r^2}{4t^2} Z(\xi), \end{aligned} \tag{32}$$

where c is the sound speed and the dimensionless functions $G(\xi)$, $V(\xi)$, and $Z(\xi)$ are related to one another by means of the following equations:

$$\xi^2 = \left[\frac{(\gamma+1)^2}{4} V(2-\gamma V)\right]^{-1} \left[\frac{(\gamma+1)}{(\gamma-1)}(\gamma V-1)\right]^{(\gamma-1)/\gamma}, \tag{33}$$

$$G = \left(\frac{\gamma+1}{\gamma-1}\right)\left[\frac{2(1-V)}{(\gamma-1)(2-\gamma V)}\right]^{2/(\gamma-2)} \left[\frac{(\gamma+1)}{(\gamma-1)}(\gamma V-1)\right]^{1/\gamma}, \tag{34}$$

$$Z = \frac{\gamma(\gamma-1)}{2}\frac{(1-V)V^2}{(\gamma V-1)}. \tag{35}$$

Eq. (33) can be solved implicitly for V using a Newton–Raphson iteration algorithm. Once the functional dependence of V with ξ is determined this way, the functions G and Z can be obtained by straightforward evaluation of Eqs. (34) and (35), respectively. The solution is completed by solving numerically the integral

$$\beta^4 = \frac{\pi}{2}\int_{1/\gamma}^{2/(\gamma+1)} \xi^4 G(V)\left[\frac{1}{2}V^2 + \frac{Z(V)}{\gamma(\gamma-1)}\right]\frac{\mathrm{d}\ln\xi}{\mathrm{d}V}\mathrm{d}V, \tag{36}$$

where the finite limit $V = 1/\gamma$ when $\xi = 0$ represents a singularity for the above integral and therefore it must be removed from the numerical integration. Numerical solution of the integral (36) gives $\beta \approx 1.0094$.

At the shock position ($\xi = 1$), $V(1) = 2/(\gamma+1)$ and so from Eqs. (32), (34), and (35) it follows that

$$\begin{aligned} \rho_{\mathrm{L}}(R,t) &= \left(\frac{\gamma+1}{\gamma-1}\right)\rho_0, \\ v_{\mathrm{L}}(R,t) &= \frac{2}{(\gamma+1)}v_{sh}(t), \\ p_{\mathrm{L}}(R,t) &= \frac{2}{(\gamma+1)}\rho_0 v_{sh}^2(t), \end{aligned} \tag{37}$$

where we have used $p = c^2\rho/\gamma$ and

$$v_{sh}(t) = \frac{\mathrm{d}R(t)}{\mathrm{d}t} = \frac{R(t)}{2t}, \tag{38}$$

is the shock velocity as obtained from Eq. (31).

For this test calculation, we consider a $\gamma = 1.4$ gas of uniform density $\rho_0 = 1$ everywhere and initial pressure $p_0 = 1.0\times10^{-5}$ except at the origin ($r = 0$), which corresponds to the explosion point. Energy deposition in a single point $r = 0$ is approximated by storing a quantity of energy $e = 1$ into a small circular area of radius $r_0 = 0.025$ at the center. This raises the pressure in the small area to

$$p_0' = \frac{(\gamma-1)e}{\pi r_0^2}. \tag{39}$$

These initial parameters are the same used by Omang et al. [37], who derived an SPH formulation for curvilinear coordinates based on new kernel functions for spherically and cylindrically symmetric problems, and Owen et al. [61], who employed an adpative SPH algorithm for evolving anisotropic smoothing lengths in which the local mean interparticle spacing varies not only in time and space but also in direction as well. In passing, we note that Eq. (39) is the bursting balloon analogue energy deposition suggested by Brode [62] and represents an approximate way to model an explosive point charge. To the right of the expanding shock ($\xi > 1$), the state at any time is given by $\rho_{\mathrm{R}}(r,t) = \rho_0$, $v_{\mathrm{R}}(r,t) = 0$, and $p_{\mathrm{R}}(r,t) = p_0$.

As for the Noh's shock calculation, we choose the (r,ϕ)-plane to represent the flow. A circular area of radius $R_c = 0.30$ is filled with particles distributed along the perimeter of n concentric circles, each containing $N_j = 10j$ particles with $j = 1, 2, \ldots, n$. With this choice, the radial separation between consecutive circles

is $\Delta r = R_c/n$ and the angular interparticle distance decreases with increasing radius according to $\Delta\phi_j = \pi/(5j)$. The mass of a particle belonging to the jth circle is as given by Eq. (30), where $m_1 = \pi(\Delta r)^2\rho_0/10$ is the mass of a particle pertaining to the innermost circle ($j = 1$). As for the 1D impulsive shock test of Section 3.6, we chose $\alpha = \beta = 1$, $g_1 = g_2 = 1$, $k = 1$, $\epsilon = 0.5$, and $h_0 = 2\Delta r$. Two independent calculations were performed using 32,400 and 61,050 particles, corresponding to $n = 80$ ($\Delta r = 0.00375$) and 110 ($\Delta r = 0.0027$) concentric circles, respectively. The timestep was fixed to $\Delta t = 1.0 \times 10^{-4}$ for the low resolution calculation and to $\Delta t = 5.0 \times 10^{-5}$ for the higher resolution run.

In Fig. 10 we show the radial profiles of mass density, pressure, and velocity at time $t = 0.05$. The solid line depicts the axisymmetric exact solution, while the asterisks and open circles correspond to the numerical solution for the low (32,400 particles) and higher resolution (61,050 particles) runs, respectively. In spite of the coarse radial resolution allowed in both cases, the strong jumps in the density, pressure, and velocity are fairly well reproduced and are considerably sharper than those obtained by Omang

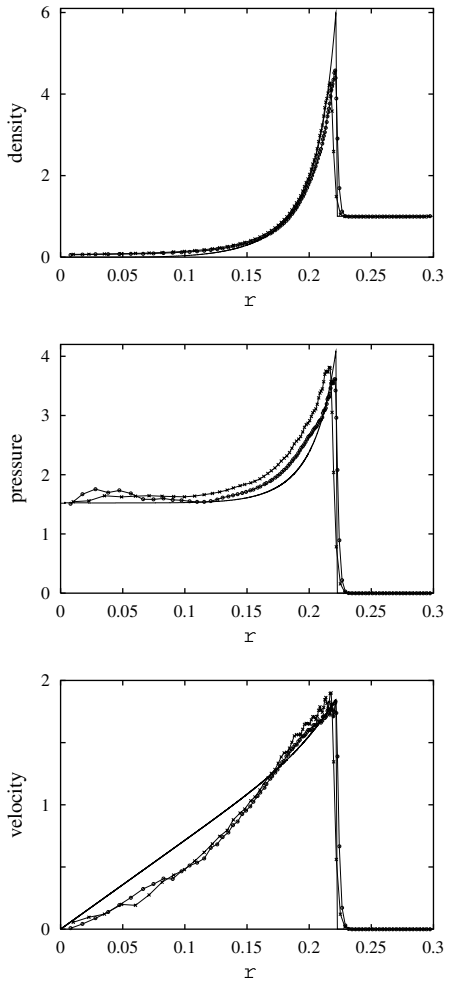

Fig. 10. Azimuthally averaged radial profiles of mass density, pressure, and radial velocity for the 2D cylindrical Sedov blast wave calculation at $t = 0.05$. The numerical profiles (asterisks: 32,400 particles; open circles: 61,050 particles) are compared to the exact solution (solid line). The location and sharpness of the shock are fairly well reproduced.

et al. [37] for the same test calculation. With comparable radial resolution, the adaptive calculations reported by Owen et al. [61] show a similarly resolved shock whose position at $t = 0.04$ is, however, slightly shifted to the right compared to the analytical solution. The calculations converge to a peak shock density of ≈4.27 and 4.57 (exact value 6) in the low and higher resolution cases, respectively. Similar peak density values were also obtained by Shashkov and Wendroff [60] using different grid refinements with their composite Lagrangian code. At $t = 0.05$, the pressure and velocity peaks are (≈3.81, ≈1.89) for the low resolution run and (≈3.60, ≈1.83) for the higher resolution calculation compared to (≈4.09, ≈1.846) for the exact solution. By $t = 0.05$ the exact shock position is at $x \approx 0.22$. As shown in Fig. 10, the higher resolution run (open circles) results in sharper shock profiles and in a better overall agreement with the exact behavior. Within the shock, the numerical profile for the density fits better the analytical solution than the pressure and velocity. This is a consequence of having approximated the intense point source of thermal energy with a finite area of radius $r_0 = 0.025$ at the center. The results are therefore dependent on the choice of this radius. According to Omang et al. [37], an increase of r_0 leads to a better convergence of the numerical velocity profile to the exact solution and a poorer fit of the density and pressure. The converse occurs if the value of r_0 is reduced. Fig. 11 displays a kernel plot at $t = 0.05$ for the higher resolution calculation. For clarity only about a quarter of the total number of particles is shown. The adaptive

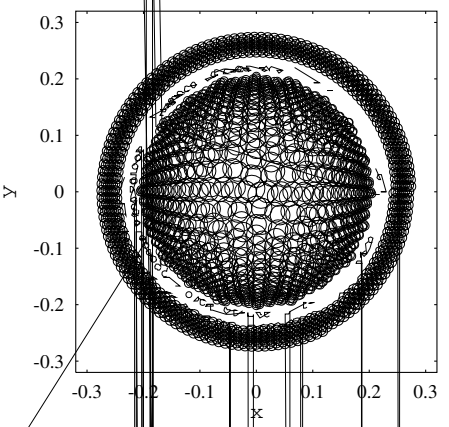

character of the kernel estimation is clearly seen by the smallest circles occurring on the shock front. It is evident that azimuthal symmetry is fairly well maintained and that the round shape of the shock front is reproduced. These features are also seen in Fig. 12, which displays a surface plot of the mass density field for the same calculation. Similar plots were also obtained for the lower resolution run. As for the impulsive load test of Section 3.6, we expect that the strength of the peak shock density will improve by using a finer radial resolution.

5. Conclusions

We have described a simple method that converts standard SPH into a working shock-capturing scheme without relying on solutions to the Riemann problem. The fluid dynamic equations are written in symmetrized SPH form and the density is obtained from the usual kernel summation so that variational consistency of the whole scheme is guaranteed [39]. The only change with respect to existing standard SPH formulations, is the implementation of an adaptive kernel estimation of the density following the procedure described by Silverman [45], which combines intrinsic features of both the kernel and the nearest neighbor approaches in a way that the amount of smoothing applied to the data is effectively controlled. In this procedure, a pilot estimate of the density is first calculated from the kernel summation. Local bandwidths corresponding to the various particles are next defined as some power of the ratio of the pilot estimates over their geometrical means, which are then used to construct the adaptive kernel estimator itself. In this way, the minimum necessary smoothing is effectively applied in regions where the density is low. While, in general, this feature improves the accuracy of the SPH method, it becomes particularly important near sharp discontinuities as in the case of phenomena involving strong shocks.

Unlike existing SPH formulations based on Riemann solvers [34–36], the adaptive kernel estimation allows for a unique scheme that handles strong shocks and rarefactions the same way. When the method is applied to high Mach number compressible flows with sharp discontinuities, the accuracy of the results is comparable, and in most cases superior, to that obtained from either Godunov-type methods or SPH formulations based on Riemann solutions. The accuracy of the method has been validated for a series of analytic, one-dimensional (1D) shock problems for which the hydrodynamical states may be either uniform or spatially varying. In particular, for problems involving infinite strength shocks, as in the blast wave [42] and wall shock test models, the method reproduced the exact solution with very good accuracy. Similarly good results were also obtained for the Sod's [41] shock-tube test and for the impulsive load problem in an inhomogeneous atmosphere [48]. The method was also seen to perform well for problems where Godunov's schemes fail such as the Roberts [43] problem, involving the propagation of a nearly stationary shock, and the Sjögreen [44] test, where two rarefaction waves move apart. The extension of the method to two dimensions was first tested against the cylindrical Noh's [49] problem in which the time evolution is an infinite strength, circularly symmetric shock moving outward. The results for this test were seen to agree reasonably well with the analytic solution, yielding a considerably less pronounced density dip at the origin compared to previously reported calculations based on either finite-difference Godunov's methods or standard SPH formulations. Sharper shock profiles for the Noh's problem would result using finer resolution. As a second stringent experiment, the method was tested against the Sedov [50] point explosion problem. In spite of the rather course radial resolution employed for this test calculation, the adaptive kernel estimation method was seen to produce a sufficiently sharp and round outgoing shock front. The agreement of the numerical solution with the exact behavior was seen to be similar to that obtained in previous calculations of the Sedov blast wave with either adaptive SPH formulations or refined finite-difference codes. We have no reasons to doubt that similar results for the tests tried here could be achieved in three dimensions provided that the calculations are performed with comparable radial resolution.

Acknowledgments

We are grateful to the anonymous referees for having provided a number of comments and clarifications that have improved both the style and content of the manuscript and for suggesting us the two-dimensional Sedov test problem. The calculations of this paper were done using the computational facilities of the Laboratories of Computational Physics and Statistical Physics of Disordered Systems of the IVIC's Physics Center. One of us (L. Di G. S.) thanks the Fondo Nacional de Ciencia, Tecnología e Innovación (Fonacit) of Venezuela for partial support.

References

[1] L.B. Lucy, A numerical approach to the testing of the fission hypothesis, Astron. J. 83 (1977) 1013.
[2] R.A. Gingold, J.J. Monaghan, Smoothed particle hydrodynamics: theory and application to non-spherical stars, Mon. Not. R Astron. Soc. 181 (1977) 375.
[3] J.J. Monaghan, Smoothed particle hydrodynamics, Annu. Rev. Astron. Astrophys. 30 (1992) 543.
[4] H. Takeda, S.M. Miyama, M. Sekiya, Numerical simulation of viscous flow with smoothed particle hydrodynamics, Prog. Theor. Phys. 92 (5) (1994) 939.
[5] H.A. Posch, W.G. Hoover, O. Kum, Steady-state shear flows via nonequilibrium molecular dynamics and smoothed-particle applied mechanics, Phys. Rev. E 52 (2) (1995) 1711.
[6] O. Kum, W.G. Hoover, H.A. Posch, Viscous conducting flows with smooth-particle applied mechanics, Phys. Rev. E 52 (5) (1995) 4899.
[7] J.P. Morris, P.J. Fox, Y. Zhu, Modeling low Reynolds number incompressible flows using SPH, J. Comput. Phys. 136 (1997) 214.
[8] W.C. Welton, Two-dimensional pdf/sph simulations of compressible turbulent flows, J. Comput. Phys. 139 (1998) 410.
[9] L. Di G. Sigalotti, J. Klapp, E. Sira, Y. Meleán, A. Hasmy, SPH simulations of time-dependent Poiseuille flow at low Reynolds numbers, J. Comput. Phys. 191 (2003) 622.
[10] E.M.D. Dalpino, A.H. Ceroqueira, 3-D sph simulations of hd and mhd jets, Astrophys. Lett. Commun. 34 (1996) 303.
[11] D.J. Price, J.J. Monaghan, Smoothed particle hydrodynamics I. Algorithm and tests in one dimension, Mon. Not. R Astron. Soc. 348 (2004) 123.
[12] D.J. Price, J.J. Monaghan, Smoothed particle hydrodynamics II. Variational principles and variable smoothing length terms, Mon. Not. R Astron. Soc. 348 (2004) 139.
[13] J.J. Monaghan, Simulating free surface flows with SPH, J. Comput. Phys. 110 (1994) 399.
[14] J.P. Morris, Simulating surface tension with smoothed particle hydrodynamics, Int. J. Numer. Meth. Fluids 33 (2000) 333.
[15] S. Nugent, H.A. Posch, Liquid drops and surface tension with smoothed particle applied mechanics, Phys. Rev. E 62 (4) (2000) 4968.
[16] A. Colagrossi, M. Landrini, Numerical simulation of interfacial flows by smoothed particle hydrodynamics, J. Comput. Phys. 191 (2003) 448.
[17] J.J. Monaghan, Implicit SPH drag and dust gas dynamics, J. Comput. Phys. 138 (1997) 801.
[18] L.D. Libersky, A.G. Petschek, T.C. Carney, J.R. Hipp, F.A. Allahdadi, High strain Lagrangian hydrodynamics, J. Comput. Phys. 109 (1993) 67.
[19] A.G. Petschek, L.D. Libersky, Cylindrical smoothed particle hydrodynamics, J. Comput. Phys. 109 (1993) 76.
[20] J.P. Gray, J.J. Monaghan, R.P. Swift, SPH elastic dynamics, Comput. Meth. Appl. Mech. Eng. 190 (2001) 6641.
[21] R.F. Stellingwerf, C.A. Wingate, Impact modeling with smooth particle hydrodynamics, Int. J. Impact Eng. 14 (1993) 707.
[22] P.W. Randles, T.C. Carney, L.D. Libersky, J.D. Renick, A.G. Petschek, Calculation of oblique impact and fracture of tungsten cubes using smoothed particle hydrodynamics, Int. J. Impact Eng. 17 (1995) 661.
[23] G.R. Johnson, R.A. Stryk, S.R. Beissel, SPH for high velocity impact computations, Comput. Meth. Appl. Mech. Eng. 139 (1996) 347.
[24] D.A. Mandell, C.A. Wingate, L.A. Schwalbe, Simulation of a ceramic impact experiment using the sphinx smooth particle hydrodynamics code, in: 16th International Symposium on Ballistics, San Francisco, CA, 23–28 September 1996.
[25] D.A. Mandell, C.A. Wingate, L.A. Schwalbe, Computational brittle fracture using smooth particle hydrodynamics, in: 14th US Army Symposium on Solid Mechanics, Myrtle Beach, South Carolina, 16–18 October 1996.
[26] J.K. Chen, F.A. Allahdadi, T.C. Carney, High-velocity impact of graphite/epoxy composite laminates, Comput. Sci. Tech. 57 (1997) 1369.
[27] C.J. Hayhurst, R.A. Clegg, Cylindrically symmetrical SPH simulations of hypervelocity impacts on thin plates, Int. J. Impact Eng. 20 (1997) 337.

[28] R.P. Swift, L.A. Behrmann, M. Halleck, K.E. Krogh, Micromechanical modeling of perforating shock damage, in: SPE 39458, The SPE Formation Damage Control Conference, Lafayette, Louisiana, 18–19 February 1998.
[29] J.W. Swegle, S.W. Attaway, On the feasibility of using smoothed particle hydrodynamics for underwater explosion calculations, Comput. Mech. 17 (1995) 151.
[30] M.B. Liu, G.R. Liu, Z. Zhong, K.Y. Lam, Computer simulation of high explosive explosion using smoothed particle hydrodynamics methodology, Comput. Fluids 32 (3) (2003) 305.
[31] P.W. Randles, L.D. Libersky, Smoothed particle hydrodynamics: some recent improvements and applications, Comput. Meth. Appl. Mech. Eng. 139 (1996) 375.
[32] J.K. Chen, J.E. Beraun, C.J. Jih, An improvement for tensile instability in smoothed particle hydrodynamics, Comput. Mech. 23 (1999) 279.
[33] G.M. Zhang, R.C. Batra, Modified smoothed particle hydrodynamics method and its application to transient problems, Comput. Mech. 34 (2004) 137.
[34] J.J. Monaghan, SPH and Riemann solvers, J. Comput. Phys. 136 (1997) 298.
[35] S. Inutsuka, Reformulation of smoothed particle hydrodynamics with Riemann solvers, J. Comput. Phys. 179 (2002) 238.
[36] S.-H. Cha, A.P. Whitworth, Implementations and tests of Godunov-type particle hydrodynamics, Mon. Not. R. Astron. Soc. 340 (2003) 73.
[37] M. Omang, S. Børve, J. Trulsen, SPH in spherical and cylindrical coordinates, preprint, 2004.
[38] J.J. Monaghan, SPH without a tensile instability, J. Comput. Phys. 159 (2000) 290.
[39] J. Bonet, T.-S.L. Lok, Variational and momentum preservation aspects of smoothed particle hydrodynamic formulations, Comput. Meth. Appl. Mech. Eng. 180 (1999) 97.
[40] B. Español, M. Revenga, Smoothed dissipativc particle dynamics, Phys. Rev. E 67 (2003) 026705-1.
[41] G.A. Sod, A survey of several finite difference methods for systems of nonlinear hyperbolic conservation laws, J. Comput. Phys. 27 (1978) 1.
[42] P. Woodward, P. Colella, The numerical simulation of two-dimensional fluid flow with strong shocks, J. Comput. Phys. 54 (1984) 115.
[43] T.W. Roberts, The behavior of flux difference splitting schemes near slowly moving shock waves, J. Comput. Phys. 90 (1990) 141.
[44] B. Einfeldt, C.D. Munz, P.L. Roe, B. Sjögreen, On Godunov-type methods near low densities, J. Comput. Phys. 92 (1991) 273.
[45] B.W. Silverman, Density Estimation for Statistics and Data Analysis, Chapman & Hall, London, 1996.
[46] A.E. Evrard, Beyond *N*-body – 3D cosmological gas dynamics, Mon. Not. R. Astron. Soc. 235 (1998) 911.
[47] L. Hernquist, N. Katz, TREESPH – A unification of SPH with the hierarchical tree method, Astrophys. J. Suppl. Ser. 70 (1989) 419.
[48] Ya.B. Zel'dovich, Yu.P. Raizer, Physics of Shock Waves and High-Temperature Hydrodynamic Phenomena, Academic Press, New York, 1967.
[49] W.F. Noh, Errors for calculations of strong shocks using an artificial viscosity and an artificial heat flux, J. Comput. Phys. 72 (1978) 78.
[50] L.I. Sedov, Similarity and Dimensional Methods in Mechanics, Academic Press Inc., New York, 1959.
[51] J.J. Monaghan, SPH meets the shocks of Noh, Monash University preprint, 1988.
[52] L. Brookshaw, Smooth particle hydrodynamics in cylindrical coordinates, ANZIAM J. 44 (E) (2003) 114.
[53] L. Hernquist, Some cautionary remarks about smoothed particle hydrodynamics, Astrophys. J. 404 (1993) 717.
[54] R.P. Nelson, J.C.B. Papaloizou, Three-dimensional hydrodynamic simulations of collapsing prolate clouds, Mon. Not. R. Astron. Soc. 265 (1993) 905.
[55] R.P. Nelson, J.C.B. Papaloizou, Variable smoothing lengths and energy conservation in smoothed particle hydrodynamics, Mon. Not. R. Astron. Soc. 270 (1994) 1.
[56] J.-M. Alimi, A. Serna, C. Pastor, G. Bernabeu, Smooth particle hydrodynamics: importance of correction terms in adaptive resolution algorithms, J. Comput. Phys. 192 (2003) 157.
[57] J.J. Monaghan, J.C. Lattanzio, A refined particle method for astrophysical problems, Astron. Astrophys. 149 (1985) 135.
[58] P. Colella, P.R. Woodward, The piecewise parabolic method (PPM) for gas dynamical simulations, J. Comput. Phys. 54 (1984) 174.
[59] K. Xu, L. Martinelli, A. Jameson, Gas-kinetic finite volume methods, flux vector splitting, and artificial diffusion, J. Comput. Phys. 120 (1995) 48.
[60] M. Shashkov, B. Wendroff, A composite scheme for gas dynamics in Lagrangian coordinates, J. Comput. Phys. 150 (1999) 502.
[61] J.M. Owen, J.V. Villumsen, P.R. Shapiro, H. Martel, Adaptive smoothed particle hydrodynamics: methodology. II, Astrophys. J. Suppl. Ser. 116 (1998) 155.
[62] H.L. Brode, Blast wave from a spherical charge, J. Appl. Phys. 26 (1955) 766.